Radiolysis of NH3:CO ice mixtures – implications for Solar system and interstellar ices

A.L.F. de Barros, A Bergantini, A Domaracka, H Rothard, P Boduch, E F Da silveira

Monthly Notices of the ROYAL ASTRONOMICAL SOCIETY

MNRAS **00,** 1 (2020)
Advance Access publication 2020 September 19

doi:10.1093/mnras/staa2865

Radiolysis of NH_3:CO ice mixtures – implications for Solar system and interstellar ices

A. L. F. de Barros [1]★ A. Bergantini,[2] A. Domaracka,[3] H. Rothard,[3] P. Boduch[3] and E. F. da Silveira [4]★

[1]*Departamento de Física, Centro Federal de Educação Tecnológica Celso Suckow da Fonseca, Av. Maracanã 229, 20271-110 Rio de Janeiro, RJ, Brazil*
[2]*Departamento de Engenharia Eletrônica, Centro Federal de Educação Tecnológica Celso Suckow da Fonseca, Av. Maracanã 229, 20271-110 Rio de Janeiro, RJ, Brazil*
[3]*Centre de Recherche sur les Ions, les Matériaux et la Photonique, Normandie Univ, ENSICAEN, UNICAEN, CEA, CNRS, CIMAP, F-14000 Caen, France*
[4]*Departamento de Física, Pontifícia Universidade Católica do Rio de Janeiro, Rua Marquês de São Vicente 225, 22451-900 Rio de Janeiro, RJ, Brazil*

Accepted 2020 September 15. Received 2020 September 15; in original form 2020 July 31

ABSTRACT

Experimental results on the processing of NH3:CO ice mixtures of astrophysical relevance by energetic (538 MeV $^{64}Ni^{24+}$) projectiles are presented. NH_3 and CO are two molecules relatively common in interstellar medium and Solar system; they may be precursors of amino acids. ^{64}Ni ions may be considered as representative of heavy cosmic ray analogues. Laboratory data were collected using mid-infrared Fourier transform spectroscopy and revealed the formation of ammonium cation (NH_4^+), cyanate (OCN^-), molecular nitrogen (N_2), and CO_2. Tentative assignments of carbamic acid (NH_2COOH), formate ion ($HCOO^-$), zwitterionic glycine ($NH_3^+CH_2COO^-$), and ammonium carbamate ($NH_4^+NH_2COO^-$) are proposed. Despite the confirmation on the synthesis of several complex species bearing C, H, O, and N atoms, no N–O-bearing species was detected. Moreover, parameters relevant for computational astrophysics, such as destruction and formation cross-sections, are determined for the precursor and the main detected species. Those values scale with the electronic stopping power (S_e) roughly as $\sigma \sim a\, S_e^n$, where $n \sim 3/2$. The power law is helpful for predicting the CO and NH_3 dissociation and CO_2 formation cross-sections for other ions and energies; these predictions allow estimating the effects of the entire cosmic ray radiation field.

Key words: astrochemistry – molecular data – methods: laboratory: molecular – interplanetary medium – cosmic rays – ISM: molecules.

1 INTRODUCTION

Carbon monoxide (CO) and other volatile species can be readily used as markers of the evolutionary stage of interstellar medium (ISM) objects such as molecular clouds and regions of star formation. Similarly, a more sophisticated analysis of the evolutionary stage of ISM objects could include measurements of complex organic molecules (COMs) since the synthesis of COMs can vary both qualitatively and quantitatively upon the physical characteristics and evolutionary stage of each astrophysical object, as demonstrated by several observational, theoretical, and laboratory studies (Bergantini et al. 2018; Maffucci et al. 2018; Shingledecker et al. 2018).

In fact, COMs include a vast number of chemical species of prebiotic importance, generally containing several atoms of carbon, oxygen, hydrogen, nitrogen, and less commonly, phosphor (Turner et al. 2019), and sulphur (Pilling & Bergantini 2015). COMs are abundantly found in cold molecular clouds, regions of star formation, and in Solar system objects such as comets, asteroids, and frozen moons (Ehrenfreund & Charnley 2000). For decades now, numerous laboratory and theoretical astrophysicists have tried to understand how the physical and chemical characteristics of an astrophysical object determine which COMs – and how much of each of them – are synthesized in a specific environment based on the initial and/or present conditions. So far, there is strong experimental and theoretical evidence that most COMs are synthesized in the ISM mainly via non-equilibrium reactions initiated when cosmic rays and secondary particles interact with ice-coated interstellar grains.

In these objects, the kinetic energy of the impinging particles can trigger excited-state reaction pathways within interstellar ices at temperatures as low as 10 K (Bergantini et al. 2018); other relevant phenomena are also induced, as for instance, shock wave expansion, sputtering, grain heating, and evaporation (e.g. Watson & Salpeter 1972; Allamandola, Sandford & Valero 1988; Gerlich 1993).

The goal of this work is to investigate the synthesis of COMs in conditions similar to those found in molecular clouds as well as in comets and frozen objects of the Solar system. This is achieved by exploiting the interaction of heavy and highly energetic ions (538 MeV $^{64}Ni^{24+}$) with an astrophysical model ice formed by two inorganic species – carbon monoxide and ammonia ($CO{:}NH_3$) – in a Fourier transform infrared (FTIR) spectroscopic study.

CO is one of the most abundant carbon-bearing molecules found in cold interstellar environments and has been observed as a constituent of molecular clouds in the gas phase (Wilson, Jefferts & Penzias 1970; d'Hendecourt & Jourdain de Muizon 1986; Menella et al. 2006) as well as in the icy mantle of interstellar grains (Soifer et al. 1979; De Graauw et al. 1996). Other than molecular hydrogen, CO is the most abundant interstellar species in the gas phase (Winnewisser

★ E-mail: ana.barros@cefet-rj.br (ALFdB); enio@vdg.fis.puc-rio.br (EFdS)

& Ungerechts 1992). Because of its abundance and low sublimation point, the ice/gas ratio of CO can be used to accurately trace the distribution of material in dense cores (Öberg et al. 2005; Seperuelo et al. 2010). Additionally, the depletion of gas-phase CO is generally associated with the adsorption on to interstellar grains caused by the temperature decrease related to the collapse of a pre-stellar core (Aikawa et al. 2001, 2008). The opposite effect is also observed: Young stellar objects trigger the sublimation of the surrounding ices, which releases CO and other volatile components into the gas phase (Talbi & Herbst 2002). Bennet, Jamieson & Kaiser (2009) have demonstrated that isolated CO molecules in astrophysical model ices exposed to energetic particles are able to undergo unimolecular decomposition to give suprathermal carbon and oxygen.

In turn, atoms of both elements participate in the synthesis of several products such as ozone (O_3), carbon dioxide (CO_2), and the ubiquitous formyl radical (HCO^+), an ion that occupies a cornerstone position in the ion–molecule chemistry (Watson 1974).

Ammonia (NH_3) is a building block in biologically important molecules such as the proteinogenic amino acids that encode for protein synthesis in eukaryotes. Indeed, almost all the proteinogenic amino acids carry the amino (NH_2) moiety [e.g. alaninde ($C_2H_4(NH_2)COOH$), Valine ($C_4H_8(NH_2)COOH$), Leucine ($C_5H_{10}(NH_2)COOH$), etc.], the only exception being Proline, which has the NH group in its structure instead]. Ammonia is among the most extensively observed species in the ISM (Ho & Townes 1983; Schmidt et al. 2016), being detected in solid and gas phases in several ISM objects (Bell et al. 1982; Knacke et al. 1982; Salinas et al. 2016).

Ammonia is commonly detected in the Solar system in the atmospheres of all the gas giant planets (Hofstadter & Muhleman 1989; Lindal 1992; Atreya et al. 2003), and is a constituent of the surface ice of satellites such as Miranda, Mimas, Enceladus, Tethys, and Rhea (Whittet et al. 2001; Bauer et al. 2002; Emery et al. 2005). Because of the possible link between the availability of NH_3 and the synthesis of amino acids in frozen astrophysical objects (Bergantini et al. 2014), here we have focused on the (tentative) detection of NH_2-bearing (amino group) species, with special attention to carbamic acid (NH_2COOH) and glycine (NH_2CH_2COOH).

Carbamic acid is considered the simplest unstable amino acid, since it only contains one amino group and one carboxylic acid (COOH) group (Chen et al. 2007), whereas glycine is considered the simplest stable amino acid. The connection between the existence of interstellar amino acids and the emergence of life has been extensively contemplated in the literature (e.g. Bernstein et al. 2002, and references). Only few studies on the formation of carbamic acid in astrophysical environments exist so far, as this species is difficult to be characterized in laboratory. Even though carbamic acid (NH_2COOH) has not been detected in the ISM yet, some studies have indicated that it can be formed within ammonia-bearing astrophysical ices both via non-thermal processes using UV radiation (Khanna & Moore 1999; Chen et al. 2007; Bossa et al. 2008b) and from thermal processes initiated on icy grains (Bossa et al. 2008b).

Performing fitting of vibrational bands with Gaussians, we have tentatively assigned prebiotic species such as zwitterionic glycine ($NH_3^+CH_2COO^-$), carbamic acid (NH_2COOH), and ammonium carbamate ($NH_4^+NH_2COO^-$), along with smaller species such as carbon dioxide (CO_2), cyanate ion (OCN^-), formate ion ($HCOO^-$), ammonium (NH_4^+), and molecular nitrogen (N_2). Although results from mathematical fitting of FTIR signals are not considered irrefutable evidence of new species, the technique is a reliable and useful tool to understand spectroscopic phenomena in certain situations, such as those discussed in this work. The objective of establishing a correlation between the mathematical fit and the real phenomena was undertaken with the following criteria in mind:

(i) It is usually easier to fit any given infrared spectrum by adding several peaks to the fitting until the sum of peaks matches the actual spectrum; however, the experience shows that this approach is, in most cases, just a mathematical fluke. Therefore, in this study the fit of each section of interest was done by adding the fewest possible number of peaks that still resulted in a good fit, which was evaluated based on the calculated residual value;

(ii) A set of fitted peaks should work as an adequate starting point for the fitting of that same band in the next fluence (as this process was done for each band at every spectrum);

(iii) As the fits were done in ascending order of fluence, the central position of each fitted peak should be approximately the same as the central position of the same peak in the previous fluence (i.e. within 2 cm^{-1}). Bands that shifted more than 2 cm^{-1} relative to the same band in the previous fluence were rejected, and the process was started over.

By following these criteria, we have found results that are consistent and reliable. In addition to the qualitative study, we have quantified the physicochemical evolution of the parent and daughter species formed within the sample as a function of fluence to determine parameters relevant to astrophysical models, such as destruction and formation cross-sections of the species. Our results show that the destruction cross-section was found to be a function of the electronic stopping power (S_e) roughly as $\sigma \sim a\, S_e^n$, where $n \sim 3/2$; these predictions allow for a comprehensive estimate of the effects caused by the cosmic ray radiation field. The results are discussed in the light of their relevance to the chemical evolution of ices in the ISM and Solar system.

2 EXPERIMENTAL

The experiments were carried out in a high vacuum chamber (10^{-8} mbar) at the IRRSUD beamline of the French National Heavy Ion Accelerator (GANIL – Grand Accélérateur National d'Ions Lourds). A detailed description of the experimental apparatus can be found in, e.g. de Barros et al. (2011a, b, c). Briefly, the NH_3:CO sample was deposited on a cesium iodide (CsI) substrate attached to a cold finger cooled at 14 K by a closed cycle helium cryostat. After deposition, the sample was irradiated by 538 MeV $^{64}Ni^{24+}$ ions (8.4 MeV u^{-1}). The ion beam impinged perpendicularly on the sample at an average flux of 5.1×10^8 ion cm^{-2} s^{-1}. The final fluence of the experiment was 1.0×10^{13} ions cm^{-2}. A sweeping mechanism assured a homogeneous irradiation of the sample's surface.

The induced ice modifications were probed by a Nicolet Magna 550 FTIR Spectrometer, covering the 5000–600 cm^{-1} region at a resolution of 1 cm^{-1}. The Lambert–Beer relationship was used to calculate the column densities N of both the reactants as well as some of the products. The variation of the column density N as a function of fluence (F) was calculated by equation (1) where N is the ratio between the IR-band area S and the absorption coefficient A_v, multiplied by a constant:

$$N(F) = \ln 10 \frac{S(F)}{A_v(F)}. \quad (1)$$

To determine the thickness L of the sample (in μm), we have used equation (2):

$$L = \frac{N_0}{6.02 \times 10^{23}} \frac{M}{\rho} \times 10^4, \quad (2)$$

Table 1. Values of the initial column density N_0, layer thickness (L), molar mass (M), and mass density (ρ) for the reactants CO and NH_3. One reference band per reactant was used in the determination of N_0.

Reactant	Reference band (cm^{-1})/(μm)	L (μm)	ρ (g cm^{-3})	N_0 ($\times 10^{17}$ molec cm^{-2})	Absorption coefficient ($\times 10^{-17}$ cm $molecule^{-1}$)
CO	2138/9.39	0.49 ± 0.08	0.81[a]	7.1 ± 0.7	1.1[a, b]
^{13}CO	2090/4.78	0.49 ± 0.08	0.81[a]	0.07 ± 0.01	1.32[a, b, c]
NH_3	1062/4.68	0.21 ± 0.03	0.74[a]	10.6 ± 0.8	1.63[c]

Note. [a]Gerakines et al. (1995). [b]Jamieson, Mebel & Kaiser (2006). [c]Bouilloud et al. (2015).

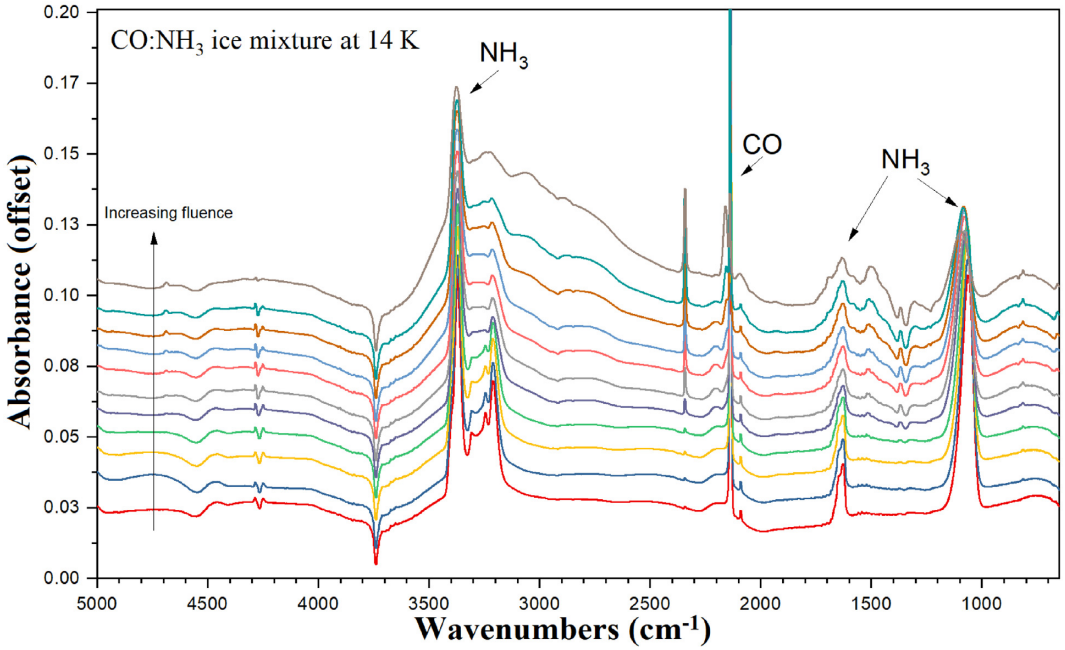

Figure 1. Evolution of the IR spectrum over the full range of fluences of the experiment. Fluence increases from bottom to top, with the lowermost spectrum corresponding to the unirradiated sample. Data are presented in the 5000–650 cm^{-1} wavenumber range. Only the main bands of the reactants are indicated in this figure.

where N_0 is the initial column density (in molecules cm^{-2}), M is its molar mass, and ρ is the mass density in solid phase as a pure substance. One IR band of reference was used for the determination of the N_0 from each reactant: The 1062 cm^{-1} band was used for NH_3 and the 2136 cm^{-1} band was used for CO. Table 1 displays the initial column density, the layer thickness, molar mass, and mass density for the precursors. Based on the parameters from Table 1, the molecular ratio of the NH_3:CO mixture was 1:0.67. The peak fitting was performed in GRAMS/AI Spectroscopy Software, version 9.2.

3 RESULTS

3.1 FTIR spectroscopy

From measuring the areas under the IR bands detected in the experiment, the initial column density (N_0) and layer thickness (L) were determined. Both N_0 and L were calculated using absorption coefficients from the literature, presented in Table 1, which also shows the reference band for each parent species, as well as their density (ρ) in amorphous ice phase. The depiction of the CO:NH_3 FTIR spectra over the entire experiment can be seen in Fig. 1, where the fluence increases from bottom to top, with the lowermost spectrum belonging to the unirradiated sample at 14 K. The most prominent IR features of NH_3 are seen in the 3500–3000 and 1700–900 cm^{-1} regions, and the intense CO and ^{13}CO bands are seen at 2136 and 2090 cm^{-1}, respectively. Two features seen at 4270 and 3740 $^{-1}$ are due to absorption by the supporting CsI substrate.

Several radiolysis products were detected by FTIR during the irradiation. Peak shifts for some of the IR bands are observed; very likely, they are caused by changes in the amorphous structure of the ice due to the nature of the heavy and energetic impinging ions, which also induces intense sputtering in the sample. To better examine the transformations within the ice sample, Fig. 2 shows the spectrum regions were IR bands, either from parent or daughter species, have been observed. The fluence of the experiment in Fig. 2 increases from bottom (0 ions cm^{-2}) To Top (1×10^{13} ions cm^{-2}). Here it is easy to notice that many IR bands are in fact the result of the overlap of multiple absorptions (e.g. Figs 2b, c, f, g, h, i, and k). It is also possible to notice that some bands shift significantly (e.g. Figs 2f, i, and k), which could be due to ice porosity loss (Loeffler, Moore & Gerakines 2016).

For this reason, the FTIR spectra are displayed in two categories: the non-overlapping bands, characterized in Table 2 and seen in Fig. 2 without asterisk, and the fitted bands, which appear with an asterisk in Fig. 2. Additionally, the fittings of the overlapping bands are shown in detail in Fig. 3 for selected fluences of the experiment, being characterized in Table 3. These results are discussed next.

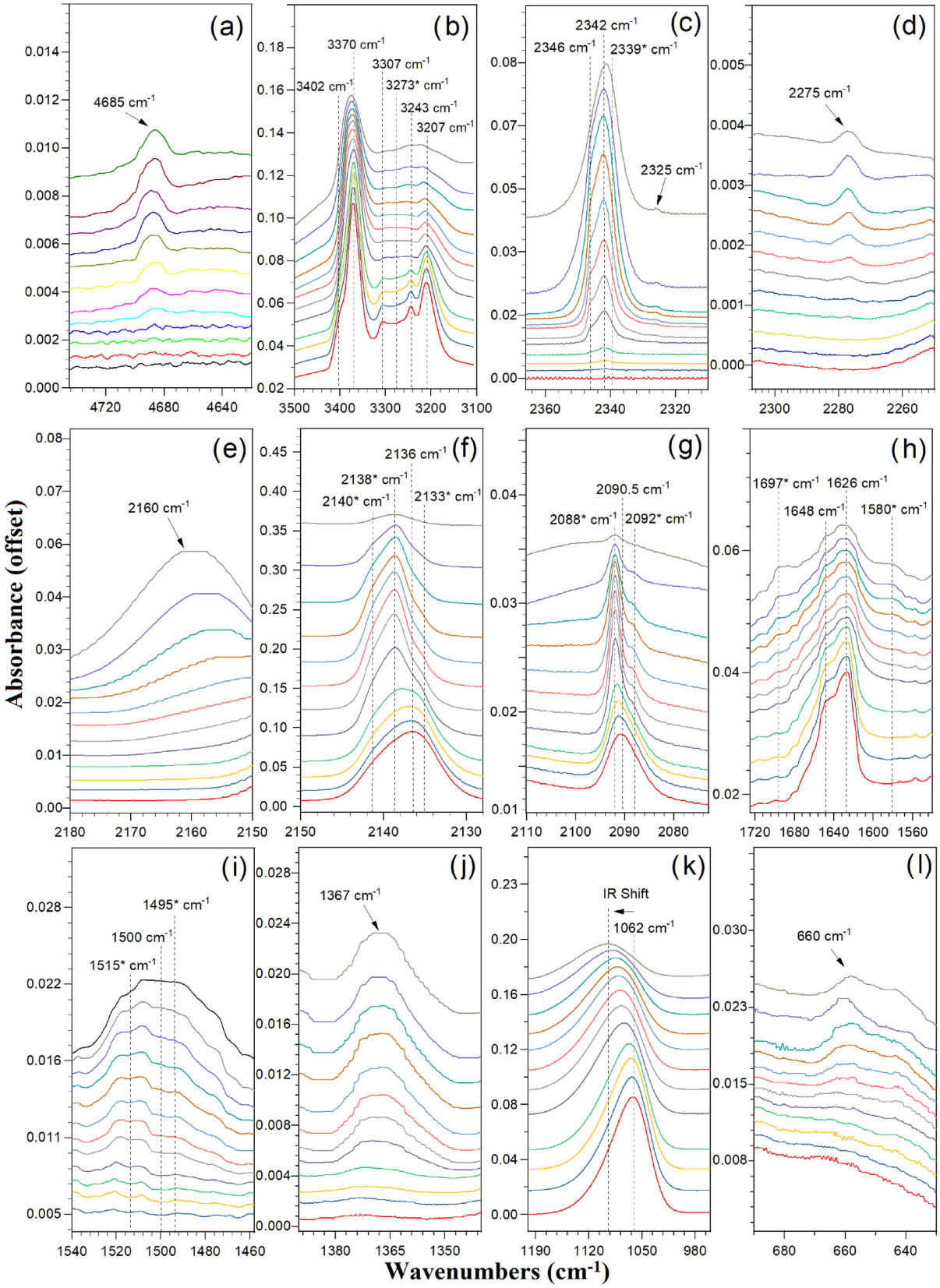

Figure 2. Detailed view of all the IR bands observed in the experiment before and during the irradiation. Fluence increases from bottom to top. The positions of the IR bands are indicated by their wavenumbers (see Table 2). Asterisk indicates overlapping bands. See Fig. 3 and Table 3 for details on these bands.

Table 2. Infrared absorption features observed before and after the irradiation of the CO:NH_3 ice mixture at 14 K.

Before irradiation (cm^{-1})	After irradiation (cm^{-1})	Assignment	Characterization	References
–	4685	$2\nu_3$ CO_2	Overtone	[1]
3402 (sh)	–	NH_3:CO	Complex	[2], [3]
3370	–	ν_3 NH_3	Sym. stretch	[4]
3307	–	$2\nu_4$ NH_3	Deformation	[3]
3243	–	NH_3	Dimer	[3]
3207	–	ν_1 NH_3	Sym. stretch	[5]
–	2346 (sh)	$(NH_3)_2$:CO_2	Complex	[6]
–	2342	ν_3 CO_2	Asym. stretch	[4]
–	2326	ν_1 N_2	N≡ N stretch	[7]
–	2275	ν_3 $^{13}CO_2$	Asym. stretch	[4]
–	2160	ν_3 OCN^-	CN stretch	[8]
2136	–	ν_1 CO	Stretch	[4]
2090 (see Table 3: 2110–2080 region)		–	–	–
1648 (sh)	–	NH_3	Trimer bending	[2]
1626	–	ν_4 NH_3	Deformation	[4], [9]
–	1500 (see Table 3: 1540–1460 region)		–	–
–	1367	-CH_3(N)	Bending δ_S	[10], [11]
1090 (see Table 3: 1190–980 region)		–	–	–
–	660	ν_2 CO_2	Bend	[4]

Note. References: [1] Bernstein, Cruikshank & Sandford (2005), [2] Bossa et al. (2008a), [3] Bossa et al. (2008b), [4] Bouilloud et al. (2015), [5] Zheng & Kaiser (2007), [6] Bertin et al. (2009), [7] Bernstein & Sandford (1999), [8] Demyk et al. (1998), [9] Ferraro, Sill & Fink (1980), [10] Schutte et al. (1999), and [11] Khanna & Moore (1999).

For example, Fig. 2(b) depicts the 3500–3100 cm^{-1} region, where several NH_3 bands occur. These are the 3402 cm^{-1} shoulder (due to the NH_3:CO complex), 3370 (ν_3), 3307 ($2\nu_4$), 3243 (NH_3 dimer), and 3207 (ν_1) cm^{-1} (see 2 for details and references). In addition to the aforementioned bands, the data fitting shows that at least one extra IR band is present in this region at 3273 cm^{-1}, which is not distinguished in experiments with similar mixtures. According to Sammes (1972), this band, seen in detail in Fig. 4, is due to a stretching mode of N–H. The Fig. 2(c) shows the predictable 2342 cm^{-1} ν_3 mode of CO_2, plus a shoulder at 2346 cm^{-1} due to (NH_3):CO_2 complexes (Bertin et al. 2009). The profile of this peak gives indication that one extra band is present. According to Figs 3(a)–(c), the fitting of the data reveals a signal at 2339 cm^{-1}, which could be due to the ν_3 mode of $C^{18}O_2$ (Maity, Kaiser & Jones 2014) or due to CO:NH_3 complexes (Altun, Bleda & Trindle 2019; Table 3). However, the most interesting peak in Fig. 2(c) is seen at 2326 cm^{-1} because, according to Bertin et al. (2009), at low temperatures and in the presence of NH_3, the infrared forbidden fundamental mode of N_2 can be enhanced enough to be detected near 2326 cm^{-1}. The fact that this band appears in the current spectra as a small, but comparatively wide peak reinforces this assignment to N_2. The bands at 2275 and 2160 cm^{-1}, seen in Figs 2(d) and (e), are from $^{13}CO_2$ and OCN^-, respectively.

The shape of the IR band at 2136 cm^{-1}, which corresponds to the ν_1 mode of CO, changes significantly throughout the experiment, as seen in Fig. 2(f). The asymmetry of this peak allows for the fitting of at least three additional signals, at 2140, 2138, and 2133 cm^{-1}. According to the literature, the 2140 and 2133 cm^{-1} bands are due to CO:NH_3 complexes (Bossa et al. 2008a) and ammonia (NH_3) complexes in argon matrix. As the fluence increases, a slight change of phase of the ice shifts the 2136 cm^{-1} CO band to 2138 cm^{-1}, creating the odd-shaped spectra seen in Fig. 2(f). Details on the fittings of this band are seen in Figs 3(d)–(f).

The asymmetry of the 2090.5 cm^{-1} band of the unirradiated ice seen in the bottom of Fig. 2(g) also indicates that more than one IR signal is present, which is made evident by the shoulder (sh) that appears as the fluence increases, and also by the blueshift at higher fluences. The fitting of the 2090.5 cm^{-1} band can be seen in Figs 3(g)–(i), which reveals two bands at 2092 and 2088 cm^{-1}, belonging to ν_1 mode of ^{13}CO and ^{18}CO, respectively. Therefore, based on literature data (see Table 3), we have concluded that although the maximum intensity of this band is found at 2090.5 cm^{-1}, it is instead comprised of two peaks at the aforementioned positions.

Another band that can be fitted with additional signals is seen in Figs 2(h) and 3(j)–(l). The bands at 1648 and 1626 cm^{-1} are assigned to a bending mode of NH_3 trimers and to ν_4 mode of NH3, respectively (see Table 2). As the fluence increases, two products appear. The first one, at 1697 cm^{-1}, attributed to νC=O mode in carbamic acid (see Table 3), is an important prebiotic species previously synthesized in similar experiments only in CO_2:NH_3 ices (Bossa et al. 2008a, b; Altun et al. 2019). A band of the other product is seen in Fig. 2(h) at 1580 cm^{-1}; it is assigned to formate ion ($HCOO^-$; Schutte et al. 1999), an important precursor of both carbamic acid and glycine (Bossa et al. 2008a; Rimola, Sodupe, & Ugliengo 2012; Nhlabatsi, Bhasi & Sitha 2016).

Features shown in Fig. 2(i) can be fitted by the sum of two peaks at 1515 and 1495 cm^{-1} (see Figs 3m–o and Table 3). Both bands are assigned, in similar experiments, to species that resemble glycine and carbamic acid. The 1515 cm^{-1} band and the 1495 cm^{-1} band are in the same region where Khanna & Moore (1999) detected zwitterion glycine ($NH_3^+CH_2COO^-$), while the 1495 cm^{-1} band was assigned to the bending mode of NH_4^+ in ammonium carbamate by Bossa et al. (2008a), Chen et al. (2007), and Schutte et al. (1999). The 1367 cm^{-1} band shown in Fig. 2(j) is assigned to the formate ion ($HCOO^-$) by Schutte et al. (1999) and Khanna & Moore (1999), an important precursor of glycine and carbamic acid.

The ν_2 mode of pure solid ammonia in thin films is normally detected at 1097 cm^{-1} (Zheng & Kaiser 2007), far from the peak detected at 1062 cm^{-1} seen in Fig. 2(k). However, this could be explained by the presence of CO in the ice mixture (Bossa et al. 2008a), although it is important to note that this band shifts considerably and gradually throughout the experiment, being centred at 1094 cm^{-1} in the final spectrum taken at the fluence of 1×10^{13} ions

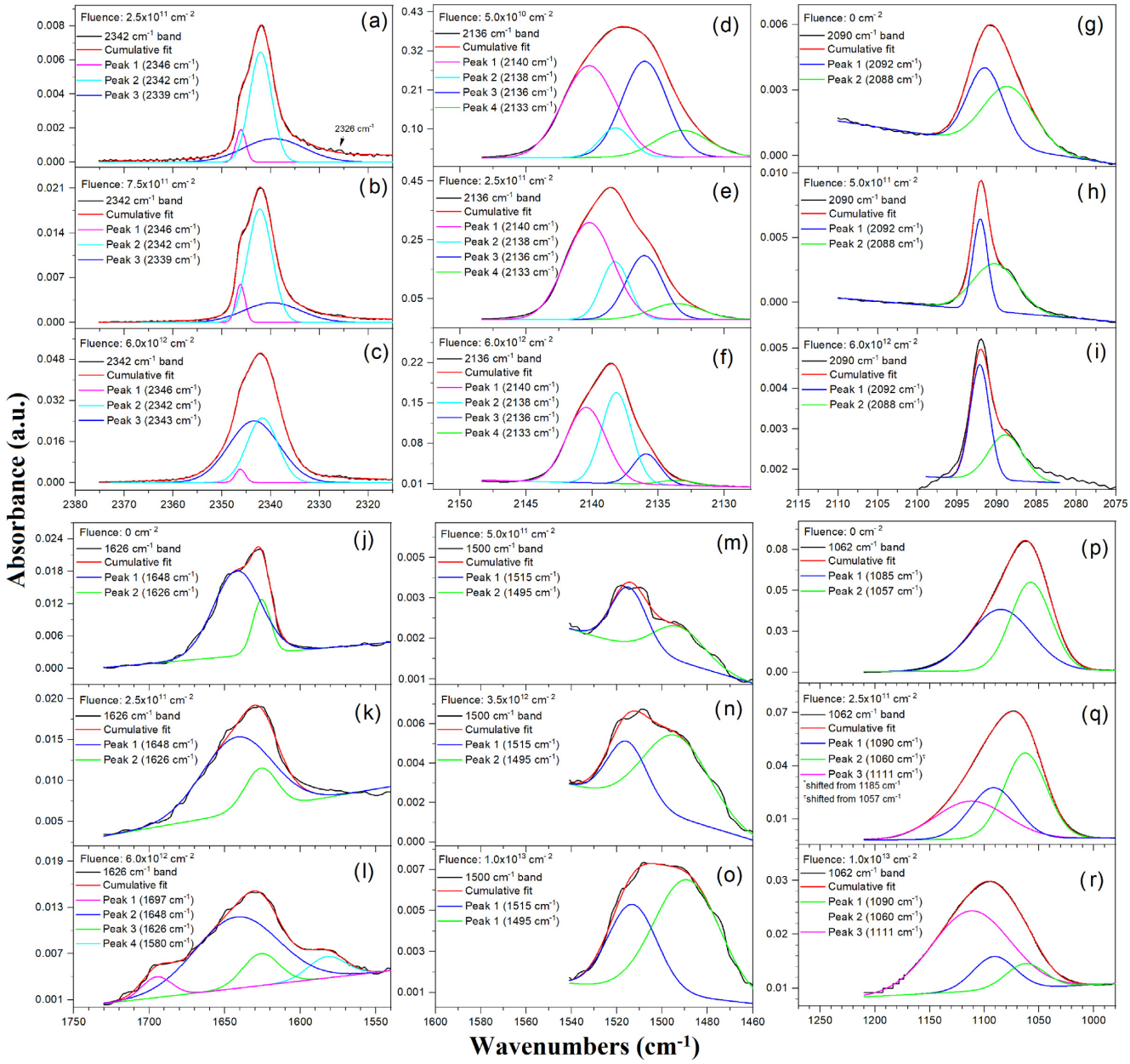

Figure 3. Gaussian fittings of the IR bands marked with asterisk in Fig. 2. For clarity, only selected fluences are shown. In each panel showing three spectra, the fluence increases from top to bottom.

cm^{-2}. To better understand these changes, we have tried innumerable parameters to fit the data across the full range of fluences of the experiment, and the most consistent results are seen in Figs 3(p)–(r) and Table 3. According to the current investigation, the asymmetrical 1062 cm^{-1} peak can be fitted as two overlapping peaks centred at 1085 and 1057 cm^{-1} (Fig. 2p). We believe that these peaks are due to the coexistence of two different phases (i.e. cubic and amorphous) of solid NH_3 (Ferraro et al. 1980; Zheng & Kaiser 2007).

However, as fluence increases, the 1085 and 1057 cm^{-1} peaks shift to 1090 and 1060 cm^{-1}, respectively, which could be explained by ice porosity loss (Loeffler et al. 2016), a common occurrence in samples exposed to irradiation. Additionally, a new band appears at 1111 cm^{-1} (see Figs 3q and r). The absorbance of this band increases with the fluence, which shows that it is a daughter species. In the literature, this band is assigned to zwitterion glycine by Khanna & Moore (1999) and to ammonium carbamate by Bossa et al. (2008b). Finally, the band at 660 cm^{-1} (Fig. 2l; Table 2) is due to the ν_2 mode of CO_2.

Therefore, based on the presented results, we suggest a (simple) reaction mechanism for the synthesis of carbamic acid within the CO:NH_3 sample. A tentative reaction mechanism begins with the direct dissociation of the reactants due to cosmic rays (ζ):

$$NH_3 \rightarrow^{\zeta} NH_2^{\bullet} + H^{\bullet} \quad (3)$$

$$CO \rightarrow^{\zeta} C + O, \quad (4)$$

where the radicals are marked with dots. Then, simplest way to produce carbamic acid within our sample would be via $NH_2CO^{\bullet}$

Table 3. Infrared absorption features of fitted peaks recorded before, during, and after irradiation of the CO:NH_3 ice mixture at 14 K.

IR region (cm^{-1})	Fitted peaks (cm^{-1})	Assignments	Characterizations	References
3500–3100	3273 (Parent)	NH_4^+	δ_s	[1], [2]
2360–2320	2339 (Daughter)	$C^{18}O_2$	ν_3	[3]
	2140 (Parent)	CO:NH_3	Complex	[4], [5]
2150–2130	2138 (Parent)	CO	ν_1	[6]
	2133 (Parent)	CO:NH_3	Complex	[4]
2110–2080	2092 (Parent)	^{13}CO	ν_1	[7]
	2088 (Parent)	$C^{18}O$	ν_1	[7]
1720–1560	1697 (Daughter)	NH_2COOH	ν C=O	[8]
	1580 (Daughter)	$HCOO^-$	COO^- Asym. stretch	[9]
1540–1460	1515 (Daughter)	$NH_3^+CH_2COO^-$	NOH bend	[10]
	1495 (Daughter)	$NH_4^+NH_2HCOO^-$	δ_s	[5], [9], [11]
	1085–1090 (Parent)	NH_3	ν_2 amorphous	[12]
1190–980	1111 (Daughter)	$NH_4^+NH_2COO^-$ and/or $NH_3^+CH_2COO^-$	$\nu_s COO^-$	[10], [11]
	1057–1060 (Parent)	NH_3	ν_2 cubic	[13]

Note. References: [1] Sammes (1972), [2] Schutte et al. (1999), [3] Maity, Kaiser & Jones (2015), [4] Bossa et al. (2008a), [5] Chen et al. (2007), [6] Bouilloud et al. (2015), [7] Maity et al. (2015), [8] Bertin et al. (2009), [9] Schutte et al. (1999), [10] Khanna & Moore (1999), [11] Bossa et al. (2008b), [12] Zheng & Kaiser (2007), and [13] Ferraro et al. (1980).

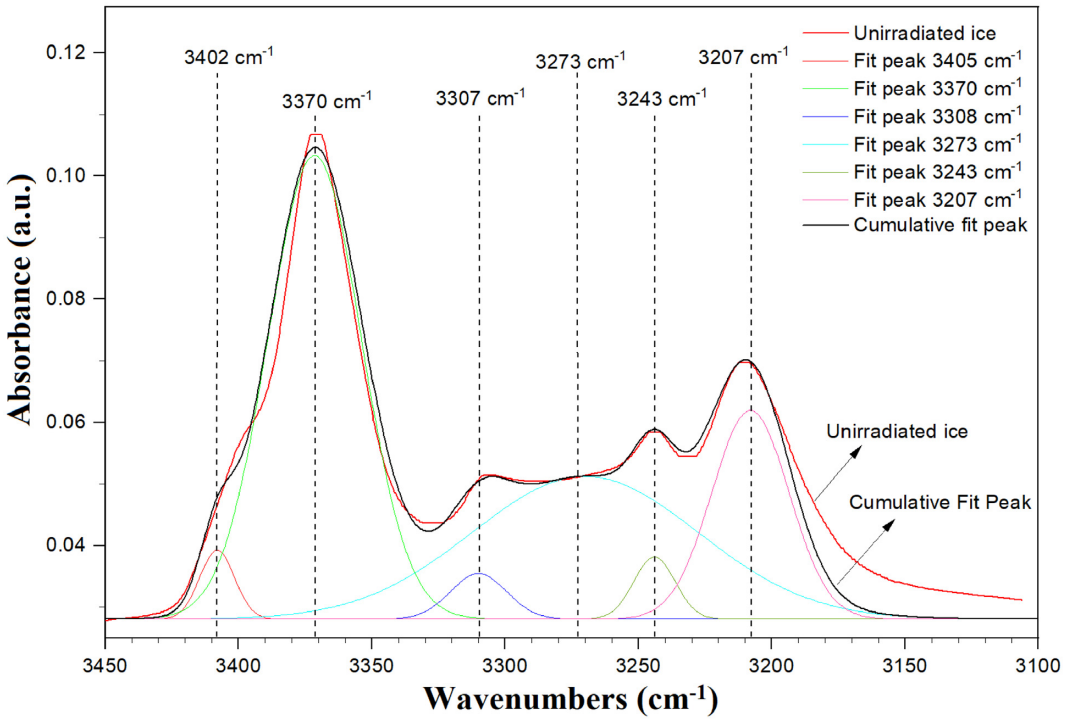

Figure 4. Gaussian fit of the IR bands in the 3450 cm^{-1} to 3100 cm^{-1} range. The assignment of the IR bands can be found in Tables 2 and 3.

(Chen et al. 2007):

$$NH_2^\bullet + CO \rightarrow NH_2CO^\bullet, \quad (5)$$

which recombines with OH (available from reactions 3 and 4):

$$NH_2CO^\bullet + OH^\bullet \rightarrow NH_2COOH. \quad (6)$$

It is possible that glycine could be produced from carbamic acid by singlet methylene $^1CH_2^{\bullet\bullet}$ insertion (Bergantini et al. 2018):

$$NH_2COOH + {}^1CH_2^{\bullet\bullet} \rightarrow NH_2CH_2COOH. \quad (7)$$

However, the preferred synthetic route to glycine within astrophysical ices, according to the literature, is via the barrierless reaction (Maeda & Ohno 2004):

$$NH_3 + {}^1CH_2^{\bullet\bullet} + CO_2 \rightarrow NH_2CH_2COOH. \quad (8)$$

Other important routes are (Chen et al. 2007)

$$NH_2^\bullet + CO \rightarrow H^\bullet + HNCO \quad (9)$$

and

$$NH_3 + HNCO \rightleftharpoons NH_4^+ + OCN^-, \quad (10)$$

which could explain the production of ammonium and cyanate within the sample.

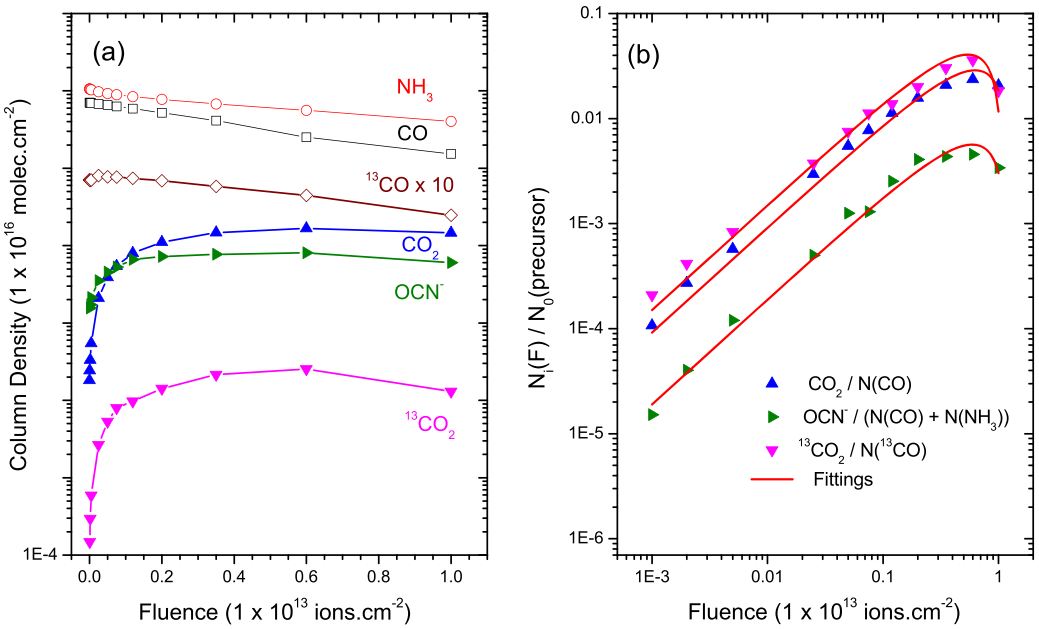

Figure 5. (a) Column-density evolution of the reactants CO and NH_3 and their products. Solid lines are aids to visualization; (b) product column density normalized to the initial column density of its precursor. The red line is the fit performed using equation (13) for the cross-section calculations.

Table 4. Destruction cross-section ($\sigma_d{}^{ap}$) of the precursor species in the mixture NH_3:CO were obtain with equation (11). The $\sigma_d{}^{ap}$ values obtained for the precursors were used to determine the formation and destruction cross-sections of the daughter species (equation 13). The constant a is used in the stopping power relationship of equation (12).

Precursor	Wavenumber (cm^{-1})	$\sigma_d{}^{ap}$ (10^{-13} cm^2)	a 10^{-18} cm^2 (keV $\mu m^{-1})^{-3/2}$
NH_3	1062	1.1 ± 0.45	1.32 ± 0.16
CO	2136	1.6 ± 0.35	0.38 ± 0.05
^{13}CO	2090	1.8 ± 0.92	–

3.2 Physical parameters

It is worth to determine physicochemical parameters relevant to the development of both chemical and astrophysical models (e.g. Herbst 1995; de Barros et al. 2015; Bergantini et al. 2018). The column density is determined by plugging the areas under the infrared bands and the absorption coefficients (A-values) from the literature in equation (1). The IR bands and A-values of reference for CO and NH_3 are listed in Table 1. For the daughter species, the reference band used for CO_2 and $^{13}CO_2$ is the ν_3 mode at 2342 and 2275 cm^{-1}, respectively, and A-values of (7.6) and (7.8) $\times$ 10^{-17} cm molecule^{-1}, respectively (Gerakines et al. 1995); the reference band for OCN^- was the ν_3 mode at 2160 cm^{-1} with an A-value of 4.0 $\times$ 10^{-17} cm molecule^{-1} (Gerakines et al. 1995). The evaluations of the column densities as a function of the fluence for the aforementioned species are displayed in Fig. 5(a). Fig. 5(b) shows the $N(F)/N_0$ ratio of the column density of the daughter species over the column density of its parent species as a function of fluence.

3.3 Precursor molecules – destruction cross-section

By applying equation (11) for each of the two precursors (reactants), and assuming a negligible variation of absorbance coefficients with fluence [i.e. $A_\nu(F)$], the destruction cross-section can be obtained as a dependence of column density on fluence:

$$N(F) = N_0 \exp[-\sigma_d^{ap} F], \tag{11}$$

where N_0 is the initial column density for each precursor (i.e. measured from the unirradiated ice – $F = 0$) and σ_d^{ap} is the apparent destruction cross-section of the parent molecule. Here, apparent means that the sputtering yield is included in the σ_d. Indeed, FTIR measures only the evolution of the intact precursors: The missing ones may disappear either by dissociation (radiolysis) or by ejection (sputtering). The evolution of the reactants' column density can be seen in the upper part of Fig. 5(a); equation (11) was used to determine the σ_d^{ap} values shown in Table 4.

3.4 Stopping power and cross-section relationship

The electronic and nuclear stopping powers (S_e and S_n, respectively) for 538 MeV $^{64}Ni^{24+}$ ions interacting with the NH_3:CO ice mixture were calculated using the TRIM code (Ziegler, Ziegler & Biersack 2010). Results are: $S_e = 2.2 \times 10^3$ keV μm^{-1}, $S_n = 1.4$ keV μm^{-1}, and penetration depth of $\sim$15 μm. Therefore, the destruction cross-section can be considered constant along the track, since the projectiles traversed the ice films with approximately constant velocity.

The dependence of the apparent destruction cross-section on the stopping power was found to be (de Barros et al. 2011b; Pereira et al. 2019)

$$\sigma_{d,f} = a S_e^n, \tag{12}$$

where a and n are constants that depend on the type of solid, being determined empirically by the analysed data (see Fig. 6). The units of S_e and $\sigma_{d,f}$ are keV μ^{-1} and cm^2, respectively. The fitting parameters for the CO and NH_3 destruction cross-sections are given in Table 4. Assuming $n = 3/2$, the parameter a values, found by best fitting, are also presented in Table 4 for CO and NH_3 precursors.

To extend the range of equation (12), literature data are included in the analysis (Moore et al. 2007; Seperuelo et al. 2009; Loeffler &

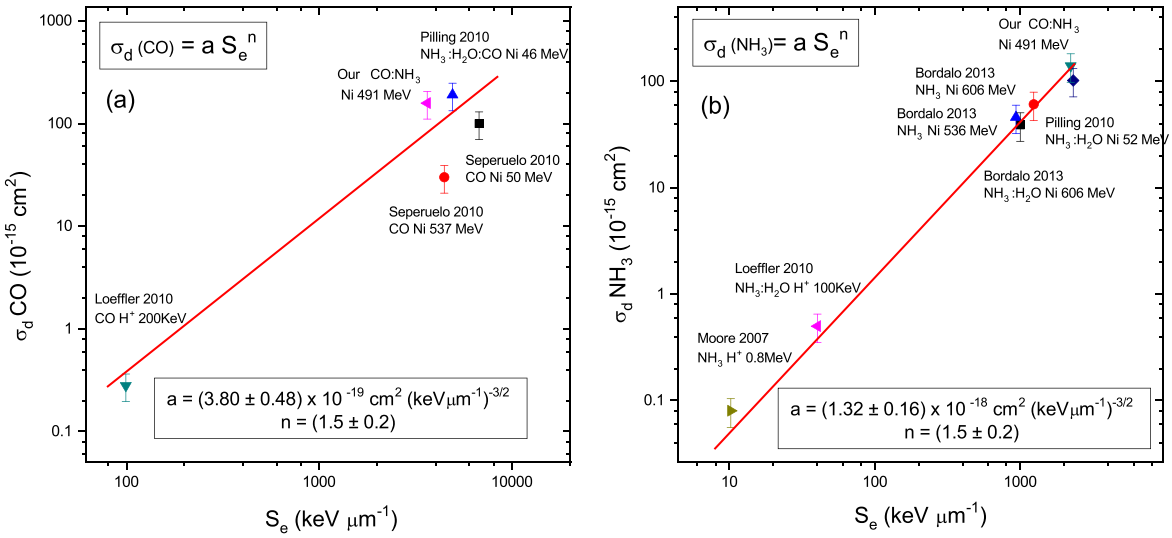

Figure 6. Apparent destruction cross-section (σ_d^{ap}) and stopping power (S_e) relationship. The power of (1.5 ± 0.2) is the relation between σd and Se for both precursor species: (a) CO and (b) NH_3. Those values were derived from this work and from those compiled from the literature.

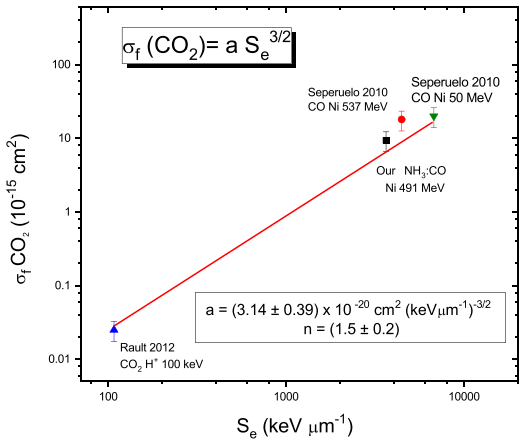

Figure 7. CO_2 formation cross-section (σ_f) and stopping power (S_e) relationship. The solid line is the function $\sigma_f = a\,S_e^n$, where $n = 1.5 \pm 0.2$. Those values were derived from this work and from those reported in literature.

Baragiola 2010; Pilling et al. 2010; Seperuelo et al. 2010; Bordalo et al. 2013, and references within); see Fig. 6. Points are scattered, but the average value $n \sim 3/2$ is reasonable. The conclusion is that molecular destruction by fast ions is an overlinear phenomenon as a function of the transferred energy rate.

Figs 6(a) and (b) show the dependence of σ_d(CO) and σ_d(NH_3), respectively, on S_e. Similar power laws have been obtained for CH_3OH and CH_4 ices (de Barros et al. 2011b) and N_2O /N_2O:CO_2 ices (Pereira et al. 2019).

Concerning the dependence on the CO_2 formation cross-sections on the stopping power dependence is depicted in Fig. 7. Effectively, $\sigma_d^{ap} \sim S_e^{3/2}$ is the trend for the CO_2 similar to results for ices reported in the literature and included in the analysis of Fig. 7 (e.g. Seperuelo et al. 2009; Seperuelo et al. 2010; Raut et al. 2012). The constant a obtained in this case is (3.14 ± 0.39) 10^{-20} cm^2 (keV μm^{-1})$^{-3/2}$.

A further discussion of the theoretical foundation and further implications of this particular scaling relation is beyond the scope of this work. However, the ensemble of results obtained with MeV ions suggests such a tight relationship (power law) between disappearance cross-sections and the electronic stopping power. The values of the exponent n of the power law are typically within the range 1.2–1.5, depending on the irradiated ice. Similar relationships for radiation effects in matter have often been reported in the material science context for ion beams ranging from keV to MeV (e.g. Papaleo et al. 1996).

3.5 Products – formation and destruction cross-sections

The column-density evolution of each product behaves according to the expression used previously in similar analyses (de Barros et al. 2011b; Pereira et al. 2018; Mejía et al. 2020):

$$N_i(F) \approx N_0 \frac{\sigma_{f,i}}{\sigma_d - \sigma_{d,i}} [\exp(-\sigma_{d,i} F) - \exp(-\sigma_d F)], \quad (13)$$

where $N_i(F)$ is the column density of the product i and N_0 is the initial column density of the parent molecule from which the product has originated. The formation and destruction cross-sections, $\sigma_{f,i}$ and $\sigma_{d,i}$, respectively, are extracted by the ratio $[N_i(F)/N_0]$ as the fluence increases. In Fig. 5(b), the solid lines correspond to equation (13) fittings, which gives the values of both formation ($\sigma_{f,i}$) and destruction $\sigma_{d,i}$ cross-sections. Because of the high energy deposited in the sample by the *Ni* projectiles, the daughter species are also subjected to destruction, which is evident in Figs 5(a) and (b) for fluences above 6×10^{12} ions cm^{-2}.

To determine these daughter species cross-sections, the initial column density N_0 (Table 1) and the destruction cross-section σ_d of the precursors (Table 4) have been used. The results are presented in Table 5.

4 DISCUSSION AND CONCLUSIONS

Surprisingly, the IR spectrum of the irradiated CO:NH_3 ice does not exhibit bands due to N–O bonds (e.g. nitrogen oxides), despite the large availability of O and N ions within the sample. So far, only four N−O-bearing species have been found in the ISM: NO, N_2O, HNO, and HONO (Coutens et al. 2019). Even though the formation mechanisms of these species in the ISM are not completely

Table 5. Formation cross-section ($\sigma_{f,i}$) and destruction cross-section ($\sigma_{d,i}$) of daughter species formed in NH_3:CO radiolysis.

Species	$\sigma_{f,i}$ (10^{-14} cm^2)	σ_{eff} (10^{-13} cm^2)	$\sigma_{d,j}$ [a] (10^{-13} cm^2)
CO_2	0.92 ± 0.08	1.79 ± 0.25	0.20 ± 0.09
$^{13}CO_2$	1.5 ± 0.5	1.85 ± 0.45	0.75 ± 0.15
OCN^-	0.19 ± 0.05	1.63 ± 0.22	0.10 ± 0.08

Note. [a] The destruction ($\sigma_{d,j}$) is defined as: $\sigma_{eff} - \sigma_{d,i}$.

known yet (Coutens et al. 2019), the current results suggest that NH_3 and CO are not the main precursors of nitrogen oxides in the ISM, a finding that is in line with that made by Martinez et al. (2014) in similar experiments. Moreover, understanding the transformations that ensue in astrophysical model ices is an important step towards the understanding of real ISM and Solar system processes. As our knowledge on this matter evolves, it becomes more challenging to discover new information, which prompts the scientific community to find device-full ways to explore the acquired data. In this work, individual absorbances were determined after fitting of experimental spectroscopic data with Gaussians. In addition, the calculation of physicochemical parameters, such as destruction and formation cross-sections of parent and daughter species due to heavy ion bombardment, yielded new information on CO:NH_3 systems, validating previous studies on the electronic stopping power relationship regarding parent species in high-energy irradiation experiments. Finally, although the fitting of experimental FTIR spectroscopic data must be interpreted carefully, our results tentatively detected carbamic acid, a species reported before in analogous experiments only in CO_2-bearing ices (exposed to thermal and/or low energy processing), in addition to glycine and ammonium carbamate. These molecules share similar structure and are a key factor in understanding how amino acids are synthesized in space, a question that may have fundamental implications for the emergence of life as we know it. Moreover, as fluence increases, the IR features in the region between 3450 and 3100 cm^{-1} (see Fig. 4), where many vibrational modes of amine-bearing species are found, become less distinctive (see Fig. 2b), making unattainable the fitting of such bands. Nevertheless, new studies exploiting complementary techniques, such as mass spectrometry (see Góbi, Bergantini & Kaiser 2017), could be exploited in future studies to verify our findings.

ACKNOWLEDGEMENTS

This work was supported by the French–Brazilian exchange programme CAPES-COFECUB. We are grateful for the support of N. N. Toribio and for the invaluable support of GANIL and CIMAP staff, in particular to T. Been, C. Grygiel, and J. M. Ramillon. The authors received financial support from CNPq in the projects: INEspaço, Bolsa de Produtividade (301868/2017-4 and 303420/2019-7), Projeto Universal (407938/2018-4), and FINEP (0647/18), and from FAPERJ in the projects: Cientista do Nosso Estado (E-245307/19) and Grupos Emergentes (E-241202/18). This study was financed in part by the Coordenação de Aperfeiçoamento de Pessoal de Nível Superior – Brasil (CAPES) – Finance Code 001, and BEX 5383/15-3. AB received financial support from the Serrapilheira Institute (Serra-1912-31853).

DATA AVAILABILITY

The data underlying this article will be shared on reasonable request to the corresponding author.

REFERENCES

Aikawa Y., Ohashi N., Inutsuka S. I., Herbst E., Takakuwa S., 2001, ApJ, 552, 639
Aikawa Y., Wakelam V., Garrod R. T., Herbst E., 2008, ApJ, 674, 984
Allamandola L. J., Sandford S. A., Valero G. J., 1988, Icarus, 76, 225
Altun Z., Bleda E., Trindle C., 2019, Life, 9, 34
Atreya S. K., Mahaffy P. R., Niemann H. B., Wong M. H., Owen T. C., 2003, Planet. Space Sci., 51, 105
Bauer H., Kasper-Giebl A., Löflund M., Giebl H., Hitzenberger R., Zibuschka F., Puxbaum H., 2002, Atmos. Res., 64, 109
Bell M. B., Kwok S., Matthews H. E., Feldman P. A., 1982, ApJ, 87, 404
Bennett C. J., Jamieson C. S., Kaiser R. I., 2009, Phys. Chem. Chem. Phys., 11, 4210
Bergantini A., Pilling S., Nair B. G., Mason N. J., Fraser H. J., 2014, A&A, 570, A120
Bergantini A., Abplanalp M. J., Pokhilko P., Krylov A. I., Shingledecker C. N., Herbst E., Kaiser R. I., 2018, ApJ, 860, 108
Bernstein M. P., Sandford S. A., 1999, Spectrochim. Acta A, 55, 2455
Bernstein M. P., Dworkin J. P., Sandford S. A., Cooper G. W., Allamandola L. J., 2002, Nature, 416, 401
Bernstein M. P., Cruikshank D. P., Sandford S. A., 2005, Icarus, 179, 527
Bertin M. et al., 2009, Phys. Chem. Chem. Phys., 11, 1838
Bordalo V., Da Silveira E. F., Lv X. Y., Domaracka A., Rothard H., Duarte E. S., Boduch P., 2013, ApJ, 774, 105
Bossa J.-B., Duvernay F., Theulé P., Borget F., Chiavassa T., 2008a, Chem. Phys., 354, 211
Bossa J.-B., Theulé P., Duvernay F., Borget F., Chiavassa T., 2008b, A&A, 492, 719
Bouilloud M., Fray N., Benilan Y., Cottin H., Gazeau M. C., Jolly A., 2015, MNRAS, 451, 2145
Chen Y.-J. et al., 2007, A&A, 464, 253
Coutens A. et al., 2019, A&A, 623, L13
de Barros A. L. F., Duarte E. S., Farenzena L. S., da Silveira E. F., Domaracka A., Rothard H., Boduch P., 2011a, Nucl. Instrum. Methods Phys. Res. B, 269, 852
de Barros A. L. F., Bordalo V. S. D. E., Duarte E. S., da Silveira E. F., Domaracka A., Rothard H., Boduch P., 2011b, A&A, 531, A160
de Barros A. L. F., Domaracka A., Andrade D. P. P., Boduch P., Rothard H., da Silveira E. F., 2011c, MNRAS, 418, 1363
de Barros A. L. F., da Silveira E. F., Bergantini A., Rothard H., Boduch P., 2015, ApJ, 810, 156
De Graauw T. et al., 1996, A&A, 315, L49
Demyk K., Dartois E., d'Hendecourt L., Jourdain de Muizon M., Heras A. M., Breitfellner M., 1998, A&A, 339, 553
d'Hendecourt L. B., Jourdain de Muizon M., 1989, A&A, 223, L5
Duarte E. S., Boduch P., Rothard H., Been T., Dartois E., Farenzena L. S., da Silveira E. F., 2009, A&A, 502, 599
Duarte E. S., Domaracka A., Boduch P., Rothard H., Dartois E., da Silveira E. F., 2010, A&A, 512, A71
Ehrenfreund P., Charnley S. B., 2000, ARA&A, 38, 427
Emery J. P., Burr D. M., Cruikshank D. P., Brown R. H., Dalton J. B., 2005, A&A, 435, 353
Ferraro J. R., Sill G., Fink U., 1980, Appl. Spectrosc., 34, 525
Gerakines P. A., Schutte W. A., Greenberg J. M., van Dishoeck E. F., 1995, A&A, 296, 810
Gerlich D., 1993, JAChS-FaTr, 89, 2199
Góbi S., Bergantini A., Kaiser R. I., 2017, ApJ, 838, 84
Herbst E., 1995, in Winnewisser G., Pelz G. C., eds, Lecture Notes in Physics, Vol. 459, The Physics and Chemistry of Interstellar Molecular Clouds. Springer, Berlin, p. 2018
Ho P. T., Townes C. H., 1983, ARA&A, 21, 239
Hofstadter M. D., Muhleman D. O., 1989, Icarus, 81, 396
Jamieson C. S., Mebel A. M., Kaiser R. I., 2006, ApJSS, 163, 184
Khanna R. K., Moore M. H., 1999, Spectrochim. Acta A, 55, 961
Knacke R. F., McCorkle S., Puetter R. C., Erickson E. F., Kratschmer W., 1982, ApJ, 260, 141
Lindal G. F., 1992, ApJ, 103, 967
Loeffler M. J., Baragiola R. A., 2010, J. Chem. Phys., 133, 214506

Loeffler M. J., Moore M. H., Gerakines P. A., 2016, ApJ, 827, 98
Maeda S., Ohno K., 2004, Chem. Phys. Lett., 398, 240
Maffucci D. M., Wenger T. V., Le Gal R., Herbst E., 2018, ApJ, 868, 41
Maity S., Kaiser R. I., Jones B. M., 2014, ApJ, 789, 36
Maity S., Kaiser R. I., Jones B. M., 2015, Phys. Chem. Chem. Phys., 17, 3081
Martinez R., Bordalo V., da Silveira E. F., Boechat-Roberty H. M., 2014, MNRAS, 444, 3317
Mejía C., de Barros A. L. F., Rothard H., Boduch P., da Silveira E. F., 2020, ApJ, 894, 132
Mennella V., Baratta G. A., Palumbo M. E., Bergin E. A., 2006, ApJ, 643, 923
Moore M. H., Ferrante R. F., Hudson R. L., Stone J. N., 2007, Icarus, 190, 260
Nhlabatsi Z. P., Bhasi P., Sitha S., 2016, Phys. Chem. Chem. Phys., 18, 20109
Öberg K. I., Van Broekhuizen F., Fraser H. J., Bisschop S. E., Van Dishoeck E. F., Schlemmer S., 2005, ApJ, 621, L33
Papaleo R. M., Hallen A., Sundqvist B. U. R., Farenzena L., Livi R. P., de Araujo M. A., Johnson R. E., 1996, Phys. Rev. B, 53, 2303
Pereira R. C., de Barros A. L. F., Fulvio D., Boduch P., Rothard H., da Silveira E. F., 2018, MNRAS, 478, 4939
Pereira R. C., de Barros A. L. F., Fulvio D., Boduch P., Rothard H., da Silveira E. F., 2019, Nucl. Instrum. Methods Phys. Res. B, 460, 249
Pilling S., Bergantini A., 2015, ApJ, 811, 151
Pilling S., Duarte E. S., da Silveira E. F., Balanzat E., Rothard H., Domaracka A., Boduch P., 2010, A&A, 509, A87
Raut U., Fulvio D., Loeffler M. J., Baragiola R. A., 2012, ApJ, 752, 159
Rimola A., Sodupe M., Ugliengo P., 2012, ApJ, 754, 24
Salinas V. N. et al., 2016, A&A, 591, A122
Sammes M. P., 1972, J. Chem. Soc. Perkin Trans., 2, 160
Schmidt M. R. et al., 2016, A&A, 592, A131
Schutte W. A. et al., 1999, A&A, 343, 966
Shingledecker C. N., Tennis J., Le Gal R., Herbst E., 2018, ApJ, 861, 20
Soifer B. T., Puetter R. C., Russell R. W., Willner S. P., Harvey P. M., Gillett F. C., 1979, ApJ, 232, L53
Talbi D., Herbst E., 2002, A&A, 386, 1139
Turner A. M. et al., 2019, Sci. Adv., 5, eaaw4307
Watson W. D., 1974, ApJ, 188, 35
Watson W. D., Salpeter E. E., 1972, ApJ, 174, 321
Whittet D. C. B., Pendleton Y. J., Gibb E. L., Boogert A. C. A., Chiar J. E., Nummelin A., 2001, ApJ, 550, 793
Wilson R. W., Jefferts K. B., Penzias A. A., 1970, ApJ, 161, L43
Winnewisser G., Kramer C., 1999, in Altwegg K., Ehrenfreund P., Geiss J., Huebner W. F., eds, Composition and Origin of Cometary Materials. Space Science Series of ISSI, Vol. 8. Springer, Dordrecht, p. 3
Zheng W., Kaiser R. I., 2007, Chem. Phys. Lett., 440, 229
Ziegler J. F., Ziegler M. D., Biersack J. P., 2010, Nucl. Instrum. Methods Phys. Res. B, 268, 1818

This paper has been typeset from a TEX/LATEX file prepared by the author.

List of astronomical key words (Updated on 2020 January)

This list is common to *Monthly Notices of the Royal Astronomical Society, Astronomy and Astrophysics*, and *The Astrophysical Journal*. In order to ease the search, the key words are subdivided into broad categories. No more than *six* subcategories altogether should be listed for a paper.

The subcategories in boldface containing the word 'individual' are intended for use with specific astronomical objects; these should never be used alone, but always in combination with the most common names for the astronomical objects in question. Note that each object counts as one subcategory within the allowed limit of six.

The parts of the key words in italics are for reference only and should be omitted when the keywords are entered on the manuscript.

General
editorials, notices
errata, addenda
extraterrestrial intelligence
history and philosophy of astronomy
miscellaneous
obituaries, biographies
publications, bibliography
sociology of astronomy
standards

Physical data and processes
acceleration of particles
accretion, accretion discs
asteroseismology
astrobiology
astrochemistry
astroparticle physics
atomic data
atomic processes
black hole physics
chaos
conduction
convection
dense matter
diffusion
dynamo
elementary particles
equation of state
gravitation
gravitational lensing: micro
gravitational lensing: strong
gravitational lensing: weak
gravitational waves
hydrodynamics
instabilities
line: formation
line: identification
line: profiles
magnetic fields
magnetic reconnection
(magnetohydrodynamics) MHD
masers
molecular data
molecular processes
neutrinos
nuclear reactions, nucleosynthesis, abundances
opacity
plasmas
polarization
radiation: dynamics
radiation mechanisms:general
radiation mechanisms: non-thermal
radiation mechanisms: thermal
radiative transfer
relativistic processes
scattering
shock waves
solid state: refractory
solid state: volatile
turbulence
waves

Astronomical instrumentation, methods and techniques
atmospheric effects
balloons
instrumentation: adaptive optics
instrumentation: detectors
instrumentation: high angular resolution
instrumentation: interferometers
instrumentation: miscellaneous
instrumentation: photometers
instrumentation: polarimeters
instrumentation: spectrographs
light pollution
methods: analytical
methods: data analysis
methods: laboratory: atomic
methods: laboratory: molecular
methods: laboratory: solid state
methods: miscellaneous
methods: numerical
methods: observational
methods: statistical
site testing
space vehicles
space vehicles: instruments
techniques: high angular resolution
techniques: image processing
techniques: imaging spectroscopy
techniques: interferometric
techniques: miscellaneous
techniques: photometric
techniques: polarimetric
techniques: radar astronomy
techniques: radial velocities
techniques: spectroscopic
telescopes

Astronomical data bases
astronomical data bases: miscellaneous
atlases
catalogues
surveys
virtual observatory tools

Software
software: data analysis
software: development
software: documentation
software: public release
software: simulations

Astrometry and celestial mechanics
astrometry
celestial mechanics
eclipses
ephemerides
occultations
parallaxes
proper motions
reference systems
time

The Sun
Sun: abundances
Sun: activity
Sun: atmosphere
Sun: chromosphere
Sun: corona
Sun: coronal mass ejections (CMEs)
Sun: evolution
Sun: faculae, plages
Sun: filaments, prominences
Sun: flares
Sun: fundamental parameters
Sun: general
Sun: granulation
Sun: helioseismology
Sun: heliosphere
Sun: infrared
Sun: interior
Sun: magnetic fields
Sun: oscillations
Sun: particle emission
Sun: photosphere
Sun: radio radiation
Sun: rotation
(Sun:) solar–terrestrial relations
(Sun:) solar wind
(Sun:) sunspots
Sun: transition region
Sun: UV radiation
Sun: X-rays, gamma-rays

Planetary systems
comets: general

comets: individual: . . .
Earth
interplanetary medium
Kuiper belt: general

Kuiper belt objects: individual: . . .
meteorites, meteors, meteoroids
minor planets, asteroids: general
minor planets, asteroids: individual: . . .
Moon
Oort Cloud
planets and satellites: atmospheres
planets and satellites: aurorae
planets and satellites: composition
planets and satellites: detection
planets and satellites: dynamical evolution and stability
planets and satellites: formation
planets and satellites: fundamental parameters
planets and satellites: gaseous planets
planets and satellites: general

planets and satellites: individual: . . .
planets and satellites: interiors
planets and satellites: magnetic fields
planets and satellites: oceans
planets and satellites: physical evolution
planets and satellites: rings
planets and satellites: surfaces
planets and satellites: tectonics
planets and satellites: terrestrial planets
planet–disc interactions
planet–star interactions
protoplanetary discs
zodiacal dust

Stars
stars: abundances
stars: activity
stars: AGB and post-AGB
stars: atmospheres
(stars:) binaries *(including multiple)*: close
(stars:) binaries: eclipsing
(stars:) binaries: general
(stars:) binaries: spectroscopic
(stars:) binaries: symbiotic
(stars:) binaries: visual
stars: black holes
(stars:) blue stragglers
(stars:) brown dwarfs
stars: carbon
stars: chemically peculiar
stars: chromospheres
(stars:) circumstellar matter
stars: coronae
stars: distances
stars: dwarf novae
stars: early-type
stars: emission-line, Be
stars: evolution
stars: flare
stars: formation
stars: fundamental parameters
(stars:) gamma-ray burst: general
(stars:) **gamma-ray burst: individual: . . .**
stars: general
(stars:) Hertzsprung–Russell and colour–magnitude diagrams
stars: horizontal branch
stars: imaging
stars: individual: . . .
stars: interiors

stars: jets
stars: kinematics and dynamics
stars: late-type
stars: low-mass
stars: luminosity function, mass function
stars: magnetars
stars: magnetic field
stars: massive
stars: mass-loss
stars: neutron
(stars:) novae, cataclysmic variables
stars: oscillations *(including pulsations)*
stars: peculiar *(except chemically peculiar)*
(stars:) planetary systems
stars: Population II
stars: Population III
stars: pre-main-sequence
stars: protostars
(stars:) pulsars: general
(stars:) **pulsars: individual: . . .**
stars: rotation
stars: solar-type
(stars:) starspots
stars: statistics
(stars:) subdwarfs
(stars:) supergiants
(stars:) supernovae: general
(stars:) **supernovae: individual: . . .**
stars: variables: Cepheids
stars: variables: Scuti
stars: variables: general
stars: variables: RR Lyrae
stars: variables: S Doradus
stars: variables: T Tauri, Herbig Ae/Be
(stars:) white dwarfs
stars: winds, outflows
stars: Wolf–Rayet

Interstellar medium (ISM), nebulae
ISM: abundances
ISM: atoms
ISM: bubbles
ISM: clouds
(ISM:) cosmic rays
(ISM:) dust, extinction
ISM: evolution
ISM: general
(ISM:) HII regions
(ISM:) Herbig–Haro objects

ISM: individual objects: . . .
(except planetary nebulae)
ISM: jets and outflows
ISM: kinematics and dynamics
ISM: lines and bands
ISM: magnetic fields
ISM: molecules
(ISM:) photodissociation region (PDR)
(ISM:) planetary nebulae: general
(ISM:) **planetary nebulae: individual: . . .**
ISM: structure
ISM: supernova remnants

The Galaxy
Galaxy: abundances
Galaxy: bulge
Galaxy: centre
Galaxy: disc
Galaxy: evolution
Galaxy: formation
Galaxy: fundamental parameters
Galaxy: general
(Galaxy:) globular clusters: general
(Galaxy:) **globular clusters: individual: . . .**
Galaxy: halo
Galaxy: kinematics and dynamics
(Galaxy:) local interstellar matter
Galaxy: nucleus
(Galaxy:) open clusters and associations: general
(Galaxy:) **open clusters and associations: individual: . . .**
(Galaxy:) solar neighbourhood
Galaxy: stellar content
Galaxy: structure

Galaxies
galaxies: abundances
galaxies: active
galaxies: bar
(galaxies:) BL Lacertae objects: general
(galaxies:) **BL Lacertae objects: individual: . . .**
galaxies: bulges
galaxies: clusters: general

galaxies: clusters: individual: . . .
galaxies: clusters: intracluster medium
galaxies: disc
galaxies: distances and redshifts
galaxies: dwarf
galaxies: elliptical and lenticular, cD
galaxies: evolution
galaxies: formation
galaxies: fundamental parameters
galaxies: general
galaxies: groups: general

galaxies: groups: individual: . . .
galaxies: haloes
galaxies: high-redshift

galaxies: individual: . . .
galaxies: interactions
(galaxies:) intergalactic medium
galaxies: irregular
galaxies: ISM
galaxies: jets
galaxies: kinematics and dynamics
(galaxies:) Local Group
galaxies: luminosity function, mass function
(galaxies:) Magellanic Clouds
galaxies: magnetic fields
galaxies: nuclei
galaxies: peculiar
galaxies: photometry
(galaxies:) quasars: absorption lines
(galaxies:) quasars: emission lines
(galaxies:) quasars: general

(galaxies:) **quasars: individual: . . .**
(galaxies:) quasars: supermassive black holes
galaxies: Seyfert
galaxies: spiral
galaxies: starburst
galaxies: star clusters: general

galaxies: star clusters: individual: . . .
galaxies: star formation
galaxies: statistics
galaxies: stellar content
galaxies: structure

Cosmology
(cosmology:) cosmic background radiation
(cosmology:) cosmological parameters
(cosmology:) dark ages, reionization, first stars
(cosmology:) dark energy
(cosmology:) dark matter
(cosmology:) diffuse radiation
(cosmology:) distance scale
(cosmology:) early Universe
(cosmology:) inflation
(cosmology:) large-scale structure of Universe
cosmology: miscellaneous
cosmology: observations
(cosmology:) primordial nucleosynthesis
cosmology: theory

Resolved and unresolved sources as a function of wavelength
gamma-rays: diffuse background
gamma-rays: galaxies
gamma-rays: galaxies: clusters
gamma-rays: general
gamma-rays: ISM
gamma-rays: stars
infrared: diffuse background
infrared: galaxies
infrared: general
infrared: ISM
infrared: planetary systems
infrared: stars
radio continuum: galaxies
radio continuum: general
radio continuum: ISM
radio continuum: planetary systems
radio continuum: stars
radio continuum: transients
radio lines: galaxies
radio lines: general
radio lines: ISM
radio lines: planetary systems
radio lines: stars
submillimetre: diffuse background
submillimetre: galaxies
submillimetre: general
submillimetre: ISM
submillimetre: planetary systems
submillimetre: stars
ultraviolet: galaxies
ultraviolet: general
ultraviolet: ISM
ultraviolet: planetary systems
ultraviolet: stars
X-rays: binaries
X-rays: bursts
X-rays: diffuse background
X-rays: galaxies
X-rays: galaxies: clusters
X-rays: general
X-rays: individual: . . .
X-rays: ISM
X-rays: stars

Transients
(transients:) black hole mergers
(transients:) black hole - neutron star mergers
(transients:) fast radio bursts
(transients:) gamma-ray bursts
(transients:) neutron star mergers
transients: novae
transients: supernovae
transients: tidal disruption events